Aeroacoustic Assessment of Porous Blade Treatment Applied to Centrifugal Fans

Journal:	*International Journal of Aeroacoustics*
Manuscript ID	IJAERO-24-0006.R2
Manuscript Type:	Original Research Article
Date Submitted by the Author:	n/a
Complete List of Authors:	Biedermann, Till; Technische Hochschule Nürnberg Georg Simon Ohm, Mechanical Engineering and Building Services Engineering Scholz, Max; Brunel University London Chong , Tze Pei; Brunel University London
Keywords:	centrifugal fan, porous structures, noise reduction, experimental modelling, destructive interference
Abstract:	Heavy-duty centrifugal fans account for a significant share of energy consumption in the process and manufacturing industries. As a result, these machines are under increasing pressure to operate at maximum efficiency to reduce costs, pollutants and noise: only combined optimization is considered competitive for future generations of fans. Preliminary studies have shown that applying structured porosity to aerofoil rear parts can lead to a reduction in self noise and trailing edge shedding noise in the mid-to-high frequency range. With this in mind, a porous surface cover is applied to a prototype centrifugal fan to evaluate the aeroacoustic potential in a complex rotating machinery. The optimal geometric characteristics of the perforation are derived from experiments with single aerofoils, while the perimeter of the covered area is varied in eight steps. The centrifugal fan specimen is rapid-prototyped and tested at different fan speeds along the complete characteristic curves, while both aerodynamic and aeroacoustic performances are simultaneously recorded. The results obtained show a significant reduction in overall noise level while aerodynamic performance is maintained. Spectral analysis shows that the noise reduction is due to a broadband effect, where the upper and lower cut-off frequencies are determined by the rotational speed and the location of the applied porosity along the blade chord. However, the maximum noise reduction is obtained as a clear function of the minimum distance between the perforation and the trailing edge of the blade, indicating that the underlying working mechanisms are a combination of broadband dissipation effects due to porosity and destructive interference.

Aeroacoustic Assessment of Porous Blade Treatment Applied to Centrifugal Fans

Abstract

Heavy-duty centrifugal fans account for a significant share of energy consumption in the process and manufacturing industries. As a result, these machines are under increasing pressure to operate at maximum efficiency to reduce costs, pollutants and noise: only combined optimization is considered competitive for future generations of fans. Preliminary studies have shown that applying structured porosity to aerofoil rear parts can lead to a reduction in self noise and trailing edge shedding noise in the mid-to-high frequency range. With this in mind, a porous surface cover is applied to a prototype centrifugal fan to evaluate the aeroacoustic potential in a complex rotating machinery. The optimal geometric characteristics of the perforation are derived from experiments with single aerofoils, while the perimeter of the covered area is varied in eight steps. The centrifugal fan specimen is rapid-prototyped and tested at different fan speeds along the complete characteristic curves, while both aerodynamic and aeroacoustic performances are simultaneously recorded. The results obtained show a significant reduction in overall noise level while aerodynamic performance is maintained. Spectral analysis shows that the noise reduction is due to a broadband effect, where the upper and lower cut-off frequencies are determined by the rotational speed and the location of the applied porosity along the blade chord. However, the maximum noise reduction is obtained as a clear function of the minimum distance between the perforation and the trailing edge of the blade, indicating that the underlying working mechanisms are a combination of broadband dissipation effects due to porosity and destructive interference.

Keywords: Aeroacoustics, Centrifugal Fans, Aerodynamics, Optimisation

Nomenclature

AoA	angle of attack, deg	TV	target values
BPF	blade passing frequency, Hz	U_0	free stream velocity, ms^{-1}
C	aerofoil chord length, mm	U_{rot}	circumferential velocity, ms^{-1}
C_P/C_0	porous coverage, %	U^*	local relative velocity, ms^{-1}
D_H	hole diameter, mm	Δp_T	rise of total pressure, Pa
D	impeller diameter, mm	$\Delta x/D_H$	chordwise hole spacing, --
f	frequency, Hz	$\Delta y/D_H$	spanwise hole spacing, --
IP	influencing parameters	ΔC	chordwise distance to the trailing edge, mm
n	rotational speed, min^{-1}	ΔS	spanwise distance between porous holes, mm
N	number of porous rows, --	δ_T	diameter number, --
(OA)SPL	(overall) sound pressure level, dB	η	efficiency (total, static), --
P_{rotor}	mechanical power, W	ρ	fluid density, kgm^{-3}
$\dot{Q}$	flow rate, m^3s^{-1}	σ_T	speed number, --
S	aerofoil span, mm	φ	flow coefficient, --
Sr	Strouhal number, --	Ψ_T	total pressure coefficient, --
T	Temperature, degC		

1. Introduction

Heavy-duty industrial fans often operate at severe ambient conditions such as dusty environments with corrosive, abrasive and adhesive media, high temperatures, high speeds and in large-scale applications. In spite of these conditions, aeroacoustic signature plays an important role: it has to meet legislative criteria, limits set by customers or it simply has to minimise its contribution as a habitat-level stressor for species. Especially if the former criteria are not met, cost-intensive silencers and absorbers are required to reduce emitted noise levels. In addition, designing low-noise fans permits running machines at higher speeds compared to the speeds of their non-optimised counterparts, constituting a clear competitive advantage. A more efficient approach than damping along the propagation path is to

reduce acoustic radiation at the source. As outlined by Eck [1] and Neise [2], the significant sources of noise of centrifugal fans can be summarised as follows:

- Interaction of mean exit flow of an impeller and volute casing, which is located at the volute cutoff and is harmonic in character (e.g. blade passing frequencies)
- Turbulent flows interacting with solid surfaces (broadband)
- Vortex shedding of impeller blade trailing edges (broadband; mid-to-high frequency)
- Secondary leakage flows through a nozzle gap (harmonic and broadband)
- Flow separation noise, for example, at the cover disk, at the impeller blades or downstream from a volute cutoff (narrowband; correlated with vortex length scales)
- Broadband impeller blade self-noise due to turbulent inflow (low-frequency) and boundary layer (mid-frequency)

As Neise [2] pointed out, the majority of aeroacoustic studies have focused on the well-understood mechanisms controlling the harmonic components of a fan's signature. Addressing turbulence-dominated broadband characteristics turns out to be quite challenging, but still represents an interesting field of research. In this regard, the specific low-noise features of owls have been of interest to the aeroacoustic community over the last decades [3,4]. Leading edge fringes to reduce turbulence ingested noise as well as serrated trailing edges are well-established features in the design of low-noise aerofoils. A third feature contributing to the low-noise profile of an owl is the downy porous coverage and permeability of its feathers, which significantly contributes to its aeroacoustic signature. Early studies on the effect of porous aerofoils were conducted by Geyer et al. [5,6]; these studies found these aerofoils had solid noise reduction but deficient aerodynamic characteristics. Successive works [7-9], however, addressed only limited porous areas on the aerofoils close to trailing edges. In these works, the results showed that there was potential to balance aeroacoustic benefits with aerodynamic penalties to a satisfactory degree. Eventually, research by Zhang and Chong [8] boosted quantifiability by employing a rapid-prototyped porosity of highly structured composition, thus avoiding the use of pre-made materials of varying topology and only limited common and thus comparable parameters. In summary, porous structures of limited extent close to the trailing edge of tested aerofoils were found to significantly attenuate radiated mid-to-high frequency noise.

To date, there are no comparable studies that address the noise reduction potential of centrifugal fans.

2. Materials and Methods

The presented research compared the aeroacoustic effects of aerofoil porosity using a single aerofoil rigidly mounted to a centrifugal industrial fan. Due to the diverse fields of application, the employed test rigs differed significantly and were thus addressed separately in *Section 2.1* and *Section 2.2*.

2.1 Aerofoil Test Rig

The current study is based on and extends previous works that statistically investigated the effect of various porous parameters on the noise reduction potential of a symmetrical aerofoil [10]. Single aerofoil experiments were conducted at the aeroacoustic test facility in Brunel University London. A low-noise wind tunnel with an open jet located in a semi-anechoic chamber of 4 m × 5 m × 3.4 m, represents optimum conditions for aeroacoustic free-field performance testing. The nozzle exit measurements were 0.1 m x 0.3 m while minimum turbulence levels were 0.1%–0.2%. Eight, ½" condenser microphones were placed in an arc at a radius of 0.97 m above the aerofoil in an equidistant distribution at angles from 50 to 120 deg, where 90 deg refers to a position perpendicular to the aerofoil midspan. This setting allowed for both area-weighted determination of sound pressure level (SPL) and determination of sound power level, independent of the distance between a source and an observer.

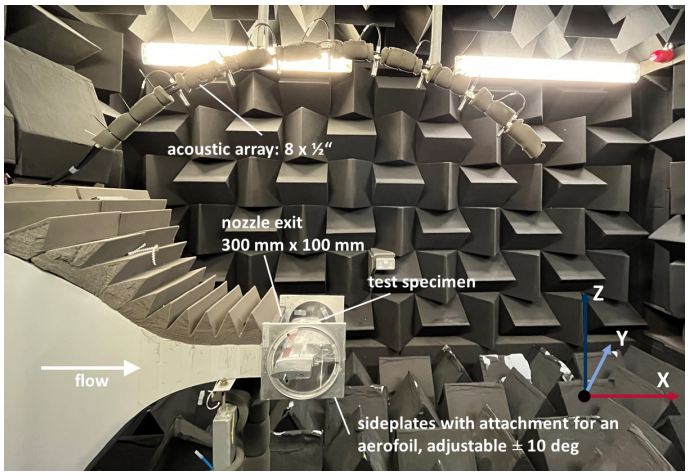

Figure 1: Picture of aerofoil test rig inside the anechoic test facility at Brunel University London. Definition of the origin of the coordinate system [11].

For the study, a NACA0012 aerofoil with a nominal chord length of $C_0 = 0.15$ m and span of $S = 0.3$ m was used and placed between the side plates as seen in Fig. 1. These plates aimed to suppress any three-dimensional effects due to the finiteness of the test body as well as allow for a continuous variation of the geometric angle of attack (AoA) in the range -10 deg ≤ AoA ≤ +10 deg. A consideration of the symmetrical features of the aerofoil neglects the potential influences of differences in the suction and pressure side of the aerofoil and hence provides most general information on the effect of porosity. The test specimen featured exchangeable rear parts, which were manufactured via rapid prototyping, had a porous pattern of variable area coverage C_P/C_0, hole diameter D_H, as well as spatial distribution in terms of span $\Delta y/D_H$ and chord $\Delta x/D_H$. Testing took place by also varying flow characteristics in terms of free stream velocity and AoA. The outer boundaries, defining the multi-dimensional experimental space, are listed in Table 1. The boundary layer was tripped on both the suction and pressure side at $x/C_0 = 0.2$ to maintain a reproducible acoustic signature based on the turbulent boundary layer.

Table 1 Parametric range, defining the 6-dimensional experimental space.

Input Parameters	X_{nondim}	Unit ----	Min -1	Mean 0	Max +1
Jet Velocity	U_0	ms^{-1}	20	40	60
Angle of Attack	AoA	deg	0	5	10
Hole Diameter	D_H	mm	0.5	1.0	1.5
Chordwise Spacing	$\Delta x/D_H$	--	1.8	3.4	5.0
Spanwise Spacing	$\Delta y/D_H$	--	1.78	4.89	8.00
Porous Coverage	C_P/C_0	%	5	15	25

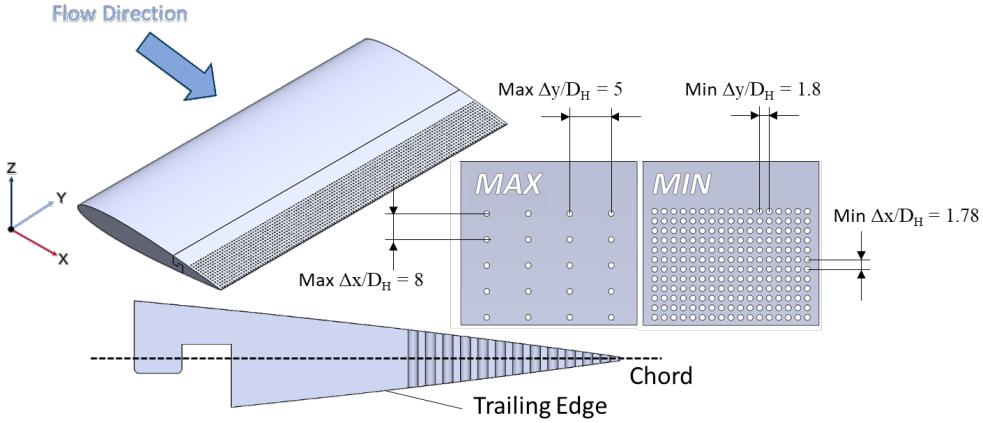

Figure 2: Section of porous blade trailing edges for NACA0012 aerofoil with 0.5 mm ≤ D_H ≤ 1.5 mm.

2.2 Fan Test Rig & Prototypes

A feasible approach to test the effect of porosity on centrifugal fans is the use of an experimental test rig: this is based on ISO 5136 [12] and ISO 5801 [13]. This approach allows for simultaneous measurements of both aeroacoustic and aerodynamic characteristics. According to the in-duct method specified by ISO 5136, a fan is installed at free inflow conditions, resulting in a pressure-side test rig. This configuration is highly realistic for various industrial applications and thus provides direct transferability of the obtained results. In general, the rig was highly similar to that described in previous studies [14]. The fan volute was equipped with an inlet nozzle to guarantee a smooth and homogeneous velocity inflow profile for the impeller, which itself was driven by an e-motor and connected via a shaft and a gauge bar to monitor torque and thus the mechanical power of the fan under investigation. Downstream, on the pressure side of the fan, the measurement of the circumferentially averaged static pressure allowed for a definition of the pressure rise of the fan, to be determined by balancing it against ambient pressure (free inflow boundary). The flow rate or dynamic pressure was measured using a high-accuracy measuring orifice located far downstream of the primary aerodynamic and aeroacoustic equipment. This location was justified because these orifices are responsible for significant pressure losses and additional noise radiation. The downstream placement of the muffler shielded against potential aeroacoustic interactions and prevented aerodynamic upstream effects, potentially affecting measurement accuracy. A similar effect applies to the detrimental acoustic influences of the throttling cone, which was needed to cover the entire characteristic curve of the tested fans. To compensate for pressure losses, an auxiliary axial fan was employed to maintain operation points at maximum flow rates as needed to test, for example, overload conditions of the centrifugal fan. In terms of operating conditions, the specific point of operation was set either by varying the rotational speed of the centrifugal fan using a frequency converter or by adjusting the position of the throttling cone at the end of the test rig. In terms of aeroacoustic signature, a ½″ Brüel & Kjær (B&K; Nærum, Denmark) condenser microphone was mounted inside a rotating duct which was connected to the static duct through elastic adapters, hence decoupling it from vibromechanical influences. In compliance with ISO 5136, rotation of this duct segment allowed for a circumferential averaging of the obtained microphone signal during measurement. To suppress potentially masking aerodynamic fluctuations on the microphone membrane, the microphone was equipped with a B&K UA0463 turbulence screen. The back reflection of the duct itself was suppressed using an anechoic termination according to ISO 5136 [12], thus enabling a continuous change in acoustic impedance.

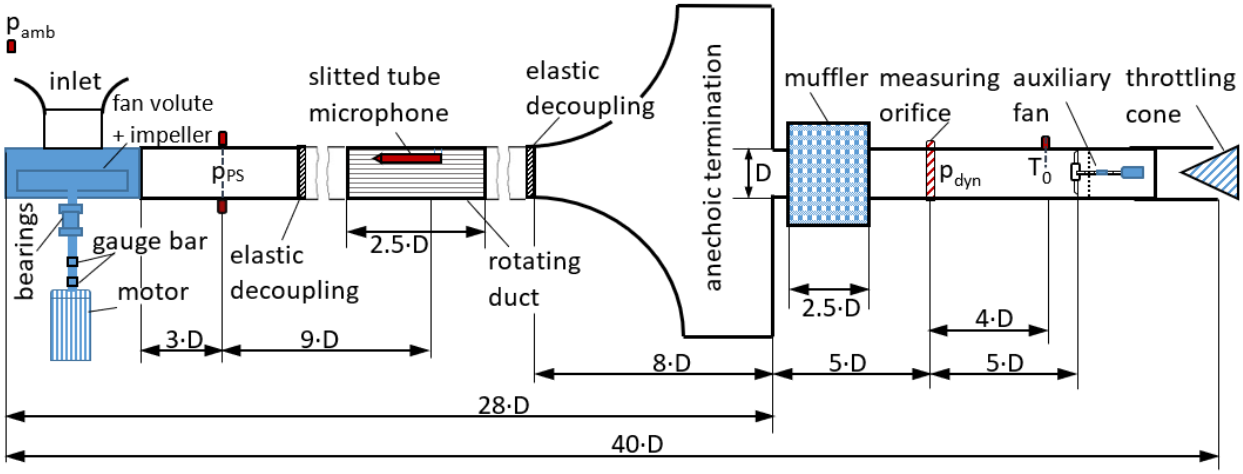

Figure 3: Experimental test rig based on ISO 5136/ ISO 5801 [12,13].

To monitor the aerodynamic and aeroacoustic performance of the prototypes, various characteristic values were defined. Aerodynamic characteristics were defined via the flow coefficient (Eq. 1) and pressure coefficient (Eq. 2), representing non-dimensional quantification of flow rate and total pressure rise, respectively, thus also allowing for a direct comparison independent of impeller diameter and/or rotational speed. These characteristics were complemented by total efficiency (Eq. 3), which compared aerodynamic power to mechanical power measured at the shaft of the fan.

Regarding aeroacoustic characteristics, it is important to distinguish between time and spectral domains. While the former provides information on total performance, the latter gives detailed insights into dominant components and allows a conclusion to be reached about potential underlying source mechanisms. A fast Fourier transformation of the aeroacoustic raw signal was performed. Eq. 4 specifies the local SPL for each spectral line in the 25 Hz ≤ f ≤ 12000 Hz range. The spectral representation also allows for additional A-weighting to account for the human perception of noise. These weighted levels are reflected in legislative upper thresholds of radiated noise and are therefore crucial for industrial acceptability of the investigated effects [15]. For the experimental studies conducted, the existing uncertainties in measurement accuracy and slight differences in adjusting the discrete points of operation naturally led to modest differences in flow rate and total pressure rise when comparing any two fans of interest. Moreover, aeroacoustic comparability is affected if the aerodynamic characteristics are not identical. Here, the aeroacoustic approach according to Madison et al. [16] allows for a direct comparison of the levels obtained for different machines, configurations and performance by incorporating the respective aerodynamic properties at a particular operation point (Eq. 5). Consequently, a characteristic curve derived from the proposed hybrid aeroacoustic approach usually shows a minimum where the product of aerodynamic efficiency and acoustic radiation is at its best. Finally, integrating or, in a value-discrete approach, summing up, the spectral lines within the covered frequency band yields the overall sound pressure level (OASPL; Eq. 6), which is equal to the OASPL based on the root-mean-squared sound pressure in the time signal. Noise reduction of both OASPL and SPL is defined by subtracting the levels of the modified prototype from those of the reference impeller (Eq. 7).

$$\varphi = \dot{Q} / U_{rot} \cdot A_{imp} \tag{1}$$

$$\psi_T = \Delta p_T / \rho \cdot (U_{rot}^2/2)^{-1} \tag{2}$$

$$\eta_T = \dot{Q} \cdot \Delta p_T / P_{Rotor} \tag{3}$$

$$SPL = 10lg(p_R^2/p_0^2);\ p_0 = 2 \cdot 10^{-5} Pa \tag{4}$$

$$SPL_{Madison} = SPL - 10lg(\dot{Q}/\dot{Q}_0) - 20lg(\Delta p/\Delta p_0) \tag{5}$$
$$\dot{Q}_0 = 1m^3/s, \Delta p_0 = 1Pa$$

$$OASPL = 10lg(\sum_{i=f_{min}}^{i=f_{max}} p_i^2/p_0^2) \tag{6}$$

$$\Delta(OA)SPL = (OA)SPL_{BSLN} - (OA)SPL_{Porous} \tag{7}$$

The acoustic signals are sampled at 32768 Hz, where 200 averages result in a measurement duration of 67s and a spectral resolution of Δf = 1 Hz. In terms of aerodynamics, sampling takes place at 25.6 kHz, resulting in a set of 768,000 samples over a measurement duration of 30 s. The microphone, resistance thermometer and shaft meter are calibrated before each measurement set while an offset correction for the manometers and an hourly update of barometric pressure and relative humidity are applied. Moreover, each remounting of the fan impeller is accompanied

by careful balancing, maintaining vibrational velocities ≤ 2 mm/s at n = 2000 min^{-1}. In terms of measurement accuracy, Table 2 indicates the averaged 95% confidence intervals of the primary aeroacoustic target quantities with the mean quantities.

Based on the preliminary studies outlined in *Section 2.1* and *Section 3*, an aeroacoustically most promising porous configuration was selected as an application for centrifugal rotating machinery: a well-proven industrial fan design was chosen from the central Bommes region which produces highly efficient centrifugal fans [17, 18]. This design featured an intermediate flow-pressure characteristic and was considered representative of a large family of centrifugal fans. The tested fan impeller was manufactured as a single piece via rapid prototyping: it had an outer diameter of 400 mm. The fan speed varied as follows along the full characteristic curve: 1000 min^{-1} ≤ n ≤ 2000 min^{-1}.

Table 2 Mean 95%-confidence intervals of experimental quantities.

Quantity	95% confidence interval	Unit
n	$\pm 1.33\% \cdot \bar{n}$	min^{-1}
ps	$\pm 1.63\% \cdot \overline{p_S}$	Pa
$\dot{Q}$	$\pm 2.80\% \cdot \bar{\dot{Q}}$	m^{3}s^{-1}
ηs	$\pm 2.07\% \cdot \overline{\eta_S}$	--
T	$\pm 0.16\% \cdot \bar{T}$	degC
SPL	$\overline{SPL} \pm 0.26$	dB

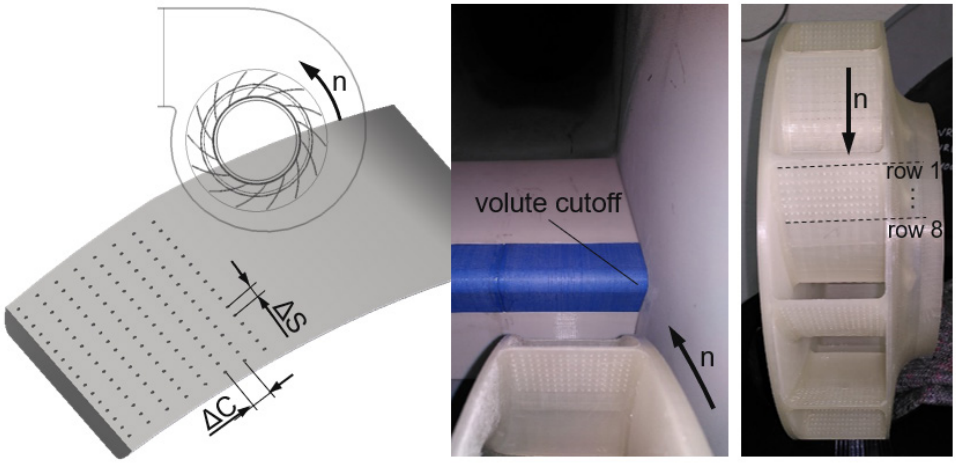

Figure 4: Impeller treatment: Single perforated impeller blade (left), impeller mounted inside its casing and connected to the exit duct (central), and impeller sideview with direction of rotation (right).

To obtain porous features, the rear impeller blade surface was covered with rows of small holes. The hole diameter was chosen to remain constant at D_H = 0.75 mm in a comparable range than for the single aerofoil experiments, documented in *Section 3*. The spanwise spacing of the holes was chosen to be $\Delta S/D_H$ = 5.3. This value combines the desired small hole diameter as indicated by the single aerofoil results ($\Delta y/D_H$) in Figure 6 (right) with the required manufacturability when applied to a 14-bladed centrifugal fan. The chordwise spacing also remained constant at $\Delta C/D_H$ = 7.5 for all the experiments conducted. Even though the single aerofoils results (Fig. 6, ($\Delta x/D_H$)) suggest minimum distances for a high noise reduction capability, the low chosen hole diameter in combination with stability restrictions results in a non-dimensional chordwise spacing far from being minimal.. The chordwise porous coverage of each fan blade varied as a function of the number of rows in a range of 5% (1 row) to 40% (8 rows, Table 3). In total, a maximum of 1792 holes were drilled into the 14 impeller blades to test the effect of structured porosity on aeroacoustic and aerodynamic performances.

Table 3 Porous coverage of impeller blades as a function of uncovered rows.

No. of Rows	Distance to TE	Porous Coverage
N	ΔC	$\%C_0$
[--]	[mm]	[%]
No Holes	0	0.0
1 Row	5.6	5.0
2 Rows	11.2	9.9
3 Rows	16.8	14.9
4 Rows	22.4	19.8
5 Rows	28.0	24.8
8 Rows (all)	44.8	39.6

3. Isolated Aerofoil Results

Based on the range of the six parameters under investigation, a statistical model featuring Box–Behnken sampling was derived. This model allowed for predicting main effects (and linear interdependencies) as functional terms up to the second order (Eq. 8), where the details of the statistical approach as well as its validation were outlined by Scholz et al. [10]. In some detail, the following Figures 5–6 highlight the general dependencies to be put into perspective with the aeroacoustic signature of the centrifugal fan (*Section 4 and 5*). Figure 5 shows a characteristic pattern of spectral noise reduction obtained by comparing a porous aerofoil to the reference aerofoil. Even though the overall sound pressure difference between the single aerofoils was found to be rather low, the spectral composition showed clear noise reduction effects of up to 4 dB in the spectral range $f_{Lower} \leq f \leq f_{Upper}$. Below f_{Lower}, the noise reduction potential corresponded to zero whereas for high frequencies ($>f_{Upper}$), an increase in aerofoil self-noise due to the holes (pores) led to a spectral increase in noise. To quantify the effect of the holes, instead of including all the surrounding noise effects, the three target values of interest were 1), the maximum local noise reduction $\Delta SPL_{f,Max}$ 2), the sum level of noise reduction $\Delta SPL_{f-Range}$ in the focus region defined by the frequency band $f_{Lower} \leq f \leq f_{Upper}$ and 3), the frequency, where maximum noise reduction occurs $f_{\Delta SPL,Max}$.

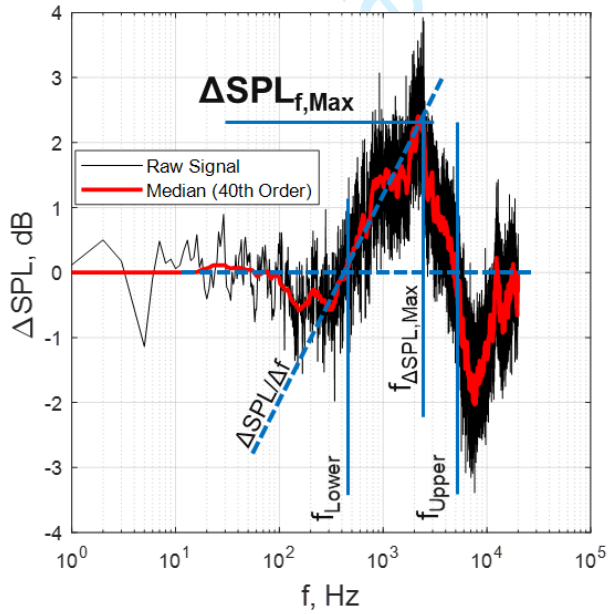

Figure 5: Spectral composition of noise reduction compared to the non-porous baseline aerofoil at U = 40 m/s, AoA = 5 deg, D =1.0, ΔX/D =3.4, ΔY/D = 4.89 and C/Co = 15%. Adopted from [10].

Based on a total of 54 tested porous cases as well as 9 non-porous baseline reference cases, a rudimentary statistical screening model was derived. To describe the target values TV with the desired accuracy, the derived statistical-

empirical model follows a functional relationship according to Equation 8, allowing each influencing parameter IP to contribute as a linear, quadratic or linearly interdependent term. Consequently, the Pareto effects in Fig. 6 (left) quantitatively show the primary terms that contribute to the three target values discussed. Positive coefficients indicate reinforcing effects and negative values refer to alleviating effects of the respective influencing parameters IP.

$$TV_i = f\left\{\sum_{j=1}^{n}\left(\left(IP_j + IP_j^2\right) + \sum_{k=1}^{n}\left(IP_j + IP_{j+k}\right)\right)\right\} \quad (8)$$
$$i = 1..3,\ j = 1..5,\ k = 1..4$$

As can be seen in Fig. 6a, the primary factors controlling peak noise reduction are the spanwise spacing of the holes (alleviating) as well as the AoA. Since both factors show alleviating characteristics, maximum noise reduction peaks require low spanwise spacing and low angles of attack. As a third major effect, the linear interdependency of free stream velocity and the hole diameter affect noise reduction in a reinforcing manner. The covered area of porosity, however, plays only a minimal role in controlling peak noise reduction.

Peak noise reduction is predominantly affected by spanwise spacing and AoA but not by the covered surface. This speaks for the primary effect being present at each individual row, showing only little streamwise interaction. On the other hand, the strong spanwise dependency hints at a certain interaction of the locally separated flow of an upstream row in a spanwise direction, before destructively interfering with the downstream row or the trailing edge, respectively. However, this is still to be validated through detailed flow measurements on the aerofoil's suction side. The required low angle of attack secures a fully attached flow regime upstream of the porous rows to retain the separation patterns in the close vicinity of the aerofoil surface. Another important set of parameters to maximise the peak noise reduction is the interdependency of the streamwise velocity and the streamwise spacing $\Delta x/C0$, which is expected to relate to the length scale of the separated vortical structure at an upstream row. According to Strouhals law, at mid-level free stream velocities (U0 = 40 m/s) and the peak noise reduction frequency ($f\Delta SPL,Max$, Fig. 5), the associated characteristic length yields L = 4 mm, being right in the range of investigated streamwise distances Δx. Furthermore, the optimum hole diameter strongly depends on the free stream velocity, hinting in a similar direction as the former aspect to enable the vortical structures to interact with the downstream holes.

The picture changes when analysing the driving parameters of the sum noise reduction along the relevant spectral range (Fig. 6b). Here, a low spanwise spacing of the hole represents the primary parameter to increase noise reduction. This was followed by low free stream velocities and low chordwise spacing of the holes. These significant differences in the main parameters were due to the need to expand the spectral range of high noise reduction as well as the amplitudes of noise reduction for high $\Delta SPL_{f\text{-}Range}$. In contrast, for $\Delta SPL_{f,Max}$, the main efforts were directed one-dimensionally to maximise the peak amplitude of the noise reduction spectra.

Allocating the maximum local noise reduction, Fig. 6c shows the most effective frequency to linearly scale with the free stream velocity in a reinforcing manner. This shows to be in line with the general spectral distribution of noise-generating mechanisms, scaling according to the Strouhal number. Particularly alleviating effects occur in combining increasing free stream velocities with high spanwise spacing of the porous holes.

The resulting trends of the discussed Pareto effects (Fig. 6 left) are exemplarily presented in Figure 6 (right). While individual parameters are varied along their full parametric range from min (-1) to max (+1), the remainders are set to optimum non-dimensional levels, being U= -1 (min), AoA= 0, D = -1 (min), $\Delta x/D$ = -1 (min), $\Delta y/D$ = -1 (min), C_P/C_0 = +1 (max). Apart from the differences in the ranking of the individual effects of the $\Delta SPL_{f,Max}$ and $\Delta SPL_{f\text{-}Range}$ in Figure 6 a-b, Figure 6 (right) proves both target values followed the same trends. For example, these values commonly showed optimum performance at a low spanwise and chordwise spacing of the holes as well as at minimum hole diameter and low free stream velocities. The covered area of porosity solely requires high values for increased noise reduction even though with less insistence. In total, a maximum local noise reduction of up to $\Delta SPL_{f,Max}$ = 6.7 dB (Fig. 6d) can be achieved, resulting in a sum level of $\Delta SPL_{f\text{-}Range}$ = 4.3 dB (Fig. 6e) in the effective spectral range and at optimum parameter settings. These results are significantly subdued due to increased noise radiation at higher frequencies, leading to maximum overall noise reduction effects of $\Delta OASPL$ = 0.5 dB on average,

though not yet including the additional potential of e.g. A-weighting for low and very high frequencies. Figure 6f illustrates the dominant effect of the free stream velocity on a spectral shift of the local noise reduction, ranging from 1 kHz – 4 kHz at maximum velocity. Comparatively, the effects of the remaining influencing parameters on the maximum reduction frequencies are low but still significant, especially for the streamwise and spanwise spacing of the holes $\Delta x/D$ ($\Delta y/D$) and the hole diameter D. The maximum noise reduction for the single aerofoil is obtained at $C_p/C_0 = 0.25$, $\Delta x/D_H = 1.8$, $\Delta y/D_H = 1.78$ and $D_H = 0.5$ mm. This applies for both the peak noise reduction as well as the sum level within the spectral focus range. The effective spectral range itself, however, primarily scales with the free stream velocity, where $U_0 = 60$ m/s results in a maximum effective frequency of 3800 Hz. As a second factor, the spanwise spacing of the pores being $\Delta y/D_H = 8.0$ also shows a contribution to an extended spectral range from 1050 Hz towards 1300 Hz.

The underlying mechanisms, which were discussed in detail by Scholz et al. [10], can be summarized as follows: especially at low angles of attack, the full blade chord was exposed to an attached flow regime, allowing an efficient destructive interplay of local upstream separation of holes versus the trailing edge separation pattern, leading to noise reduction. The low hole diameter caused only minimal aerodynamic disturbances in flow, hence keeping the generated self-noise at low levels while working aerodynamically efficiently. An increase in the covered area of porosity added to the broadband effect of the applied holes, while the primary effect was determined by the row closest to the trailing edge. A comparable effect was suggested for the chordwise spacing of the holes, while, in the spanwise direction, the number of interfering spots increased with reducing distance between any two holes. The free stream velocity, however, affected the total level of the aeroacoustic signature of an aerofoil in the stream. Given that low total values require a less significant reduction of the linear sound pressure to obtain the same logarithmic noise reduction [dB] than is the case for high reference values (Eq. 4, Eq. 7) of the aerofoils (at high free stream velocities), this parameter was only partly suitable for describing a purely aeroacoustic effect of aerofoil porosity.

Apart from the parameters defined by the aerodynamic conditions, the obtained results of the preliminary study on single aerofoils were taken into consideration when designing porous impeller blades. At the same time, however, the manufacturability of the prototypes represented additional constraints.

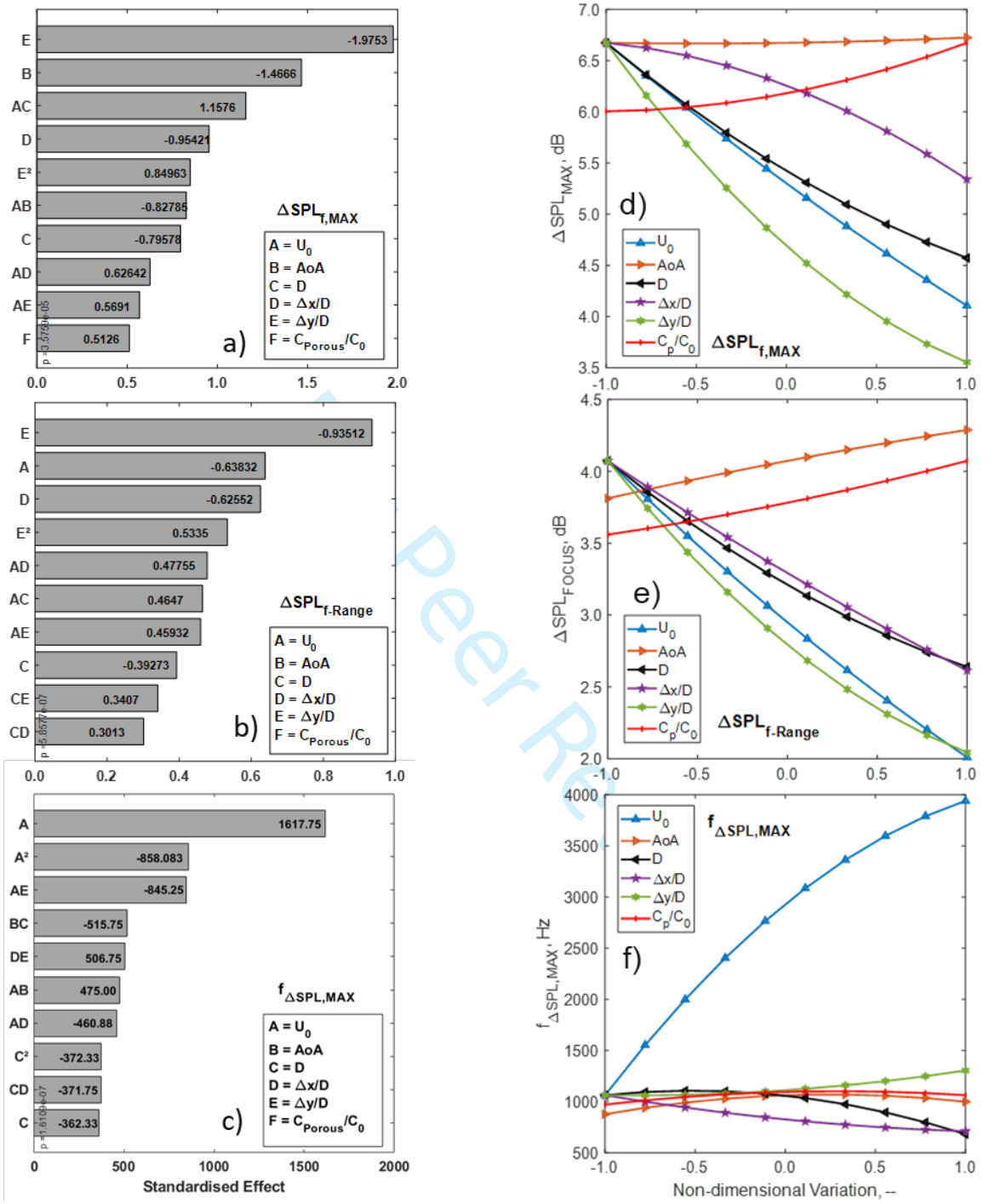

Figure 6: Parametric effect on the target quantities of a), d) the local maximum noise reduction $\Delta SPL_{f,Max}$ b), e) the cumulative noise reduction in the relevant spectral range $\Delta SPL_{f\text{-}Range}$ and c), f) of the maximum noise reduction frequencies $f_{\Delta SPL,Max}$. Left: Pareto effects (mean strength of effects) with negative values indicating alleviating effects and positive values reinforcing effects. Right: Optimum effects of the derived empirical-statistical model with non-varied parameters on their optimum levels.

4. Porous Impeller Speed Variation

The following section presents the aeroacoustic and aerodynamic results of the tested impellers with and without porous treatment. It is subdivided in the time domain into overall parameters (*Section 4.1*) such as global aerodynamics and OASPL and, on the other side, spectral results (*Section 4.2*) to uncover the underlying aeroacoustics mechanisms which cannot be derived by purely examining the resulting levels. Note that during the analysis in *Section 4*, the maximum number of porous holes was added to the impeller blades, resulting in a porous surface that was approximately 40% covered with holes.

4.1 Full Blade Comparison: Global Performance

The global aerodynamics shown in Figure 7 served two purposes. First, the impellers under investigation were tested at variable rotational speeds, where non-dimensional characteristics (Eq. 1–2) showed a collapsing pattern if the operation characteristics had equal physical conditions and no major differences such as variable separation patterns. This could be confirmed in terms of the throttling curves (pressure vs. flow coefficient), with the impeller showing minimal superior performance at maximum rotational speed for both porous and reference impellers. Regarding aerodynamic efficiency, again, a comparable characteristic was observed even though reduced efficiencies could be seen for high speeds. Even though higher fan speeds condition higher losses in the duct and casing that scale according to Bernoulli as $\Delta p \sim U^2$ [19], the total impact of these effects is expected to diminish due to the profitable effects of the Reynolds number on the internal flow. As a consequence, the reduced efficiency for high speeds as observed in Figure 7 can be ascribed to a detrimental experimental setting as outlined in more detail in *Section 5.1* (Figure 11). While conducting the experimental measurements, the first rotational speed tested was at $n = 2000\ min^{-1}$. However, since the impeller with the porous coverage was the first being tested after reassembling the test rig, the results show the impact of shaft sealing, apparently rubbing with the shaft and hence increasing the required shaft power of the electric motor as can be seen from the efficiency of the porous impeller at $n = 2000\ min^{-1}$ in Fig. 8. The static pressure rise of the tested impeller remained unperturbed since the aerodynamic characteristics were not affected. This increased friction at the shaft took place even though the setup was in operation about 15 min before starting the measurements. After the first measurements, the sealing ran free, increasing the validity of the subsequent measurements.

The second purpose was to make a direct comparison between the original reference fan performance and the porous impeller. As can be seen in Figure 7, the porous impeller continuously showed a reduced total pressure rise, which amounted to mean differences in total pressure of $\Delta(\Delta p_T) = -1.01\%$ and in efficiency of $\Delta\eta_T = -0.1\%$ along the whole characteristic curve at $n = 2000\ min^{-1}$, which was thought to be caused by the induced flow resistance due to the micro-separation effects of the added pores. Since the aerodynamic penalties appeared to be possibly negligible, there is a reason to continue an aeroacoustic assessment.

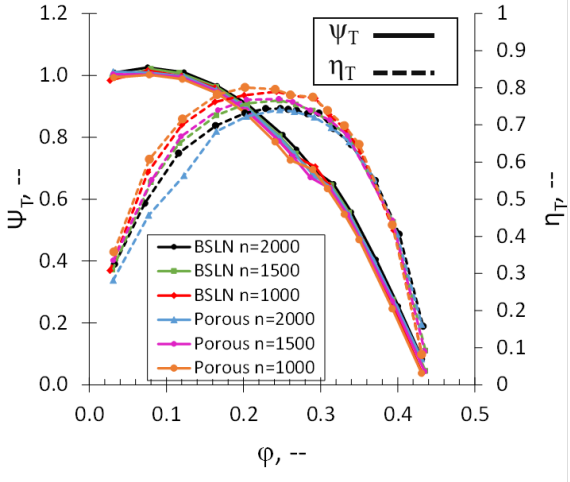

Figure 7: Aerodynamic performance comparing a fully porous configuration to a baseline case (non-porous, clean impeller) at variable fan speed and constant porous coverage $C_P/C_0 = 40\ \%$.

As discussed in Eq. 4–7, OASPL can be expressed as a representative of physical sound pressure (Fig. 8 a) by considering the human perception of noise (Fig. 8 b) or by incorporating underlying aerodynamic performance (Fig. 8 c–d) to enable a fair acoustic comparison between cases of slightly different performance in terms of pressure rise or flow rate. Figure 8 shows the general OASPL for the baseline and the porous impeller (8 rows applied; 40% porous surface) at three distinct fan speeds along the entire characteristic curve of the fan. In total measures, no significant differences are observed from Fig. 8a, while the application of spectral A-weighting (Fig. 8b) indicates clear noise reduction in all operating points ($\Delta OASPL_{Mean} = 1.57$ dB(A)): the reduction is most distinct under overload conditions ($\Delta OASPL_{Overload} = 2.47$ dB(A)). In reverse conclusion, this pattern already indicates significant noise reduction in a spectral range where human perception is sensitive (1 kHz ≤ f ≤ 6 kHz). For an acoustic analysis in comparable aerodynamic states, Figure 8d shows clear benefits under overload conditions ($\varphi \geq 0.35$) and part-load conditions ($\varphi \leq 0.2$) of the fan, where the total noise levels are generally higher than they are at design conditions. Even though Fig. 6 (a, b) indicates the (max) noise reduction is at a maximum at low angles of attack, the noise reduction increases, when all remaining parameters are set to optimum settings (Fig. 6. d, e). This pattern can be transferred to the rotating application, where at part-load the relative inflow angle is high (high AoA) and the aeroacoustic performance is at its maximum.

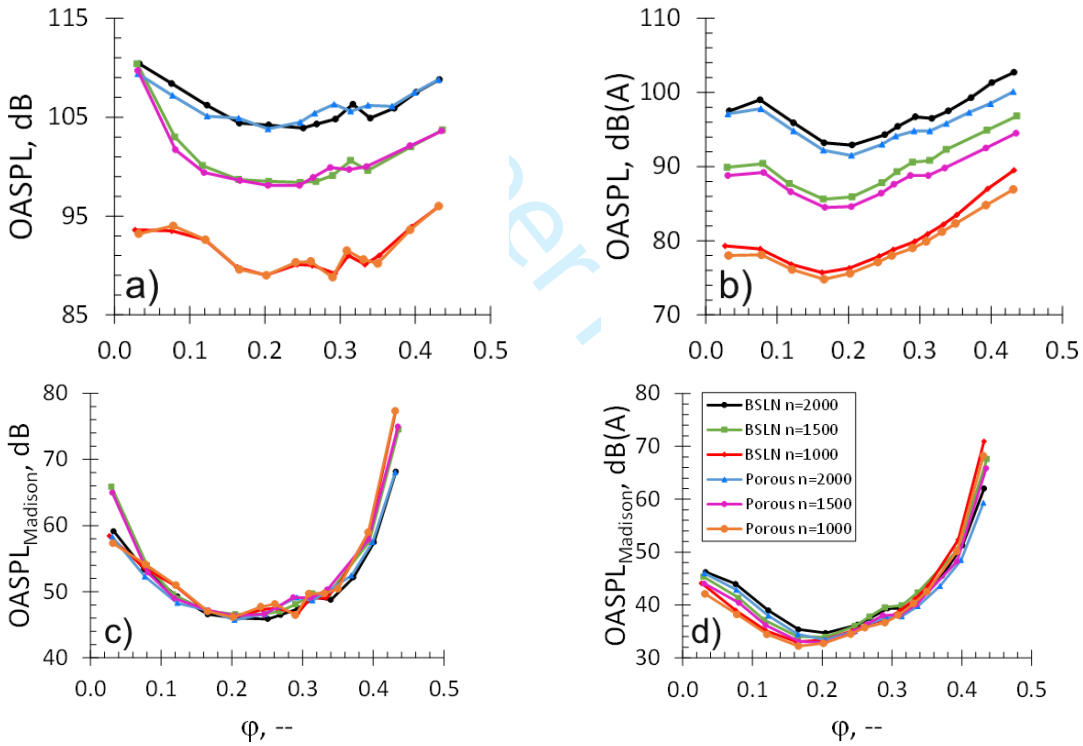

Figure 8: Overall sound pressure level, non-weighted (a,c) and A-weighted (b,d) at variable fan speed [min^{-1}] along the characteristic curve. Comparison of baseline vs. fully perforated fan blades.

4.2 Full Blade Comparison: Spectral Composition

The global acoustic pattern discussed in *Section 4.1* was broken down to its spectral composition to identify underlying mechanisms. Figure 9 clearly shows local noise reduction spectra by comparing the porous impeller versus the baseline reference case at 13 discrete flow coefficients along the characteristic curve while varying the fan speed from 2000 min^{-1} (Fig. 9; left) to 1000 min^{-1} (Fig. 9; right). Magnitudes greater than zero indicate a noise reduction in the porous impeller, whereas negative values represent a noise increase. Especially in the mid-frequency range of f ≤ 3 kHz, a significant noise reduction was observed for the porous case. Generally, local regions of maximum noise reduction can be seen surrounded by spectral regions with reduced effectiveness. This pattern remained for all

operation points and multiple fan speeds even though at n = 2000 min^{-1} and most severe part-load conditions the primary peak shifted towards low frequencies. This shift could be assigned to the suppression of local stall due to the high angles of incidence. To quantify the spectral extension of the noise reduction, a minimum frequency f_{min} was set for the first local peak (narrowband character) in terms of the noise reduction, whereas the maximum frequency f_{max} defined the peak frequency of the entire spectrum. A summary of the extracted bounds is presented in Table 4 for three different fan speeds at design conditions. However, a consideration that the underlying key effect of the noise reduction peaks was destructive interference leads to the potential scaling law proposed in Eq. 9. Two periodic signals can show interference effects, depending on their phase relations. If the signals are in phase ($\Delta\phi = 0, 2\pi, 4\pi, \ldots$), constructive interference occurs, amplifying the resulting signal. Conversely, if the signals are inversely phased, destructive interference occurs, which might even lead to an extinction of the signal if the signal amplitudes are of the same value. The required condition can be stated as $\Delta\phi = \pi$ and its odd multiples. The flow along the impeller usually sheds right at the blade trailing edge, causing significant noise radiation of intermediate to high spectral content (small structures). However, upon introducing porosity, flow locally suffers micro separation at the first row of holes, which interact with the blade trailing edge. In consequence, the more periodic the shedding at both the porous row and trailing edge are and the more the frequencies approach $\Delta\varphi = \pi$, the higher the resulting noise reduction will be. Hence, the maximum design frequency for destructive interference is determined by the minimum chordwise distance between the first porous row and the blade trailing edge in direct relation to the local flow velocity as stated in Eq. 8. Apart from the first porous row, additional rows potentially add to the broadband effect of noise reduction in terms of additional destructive interference and dissipation as discussed in detail in *Section 5*. In a stationary setup, local flow velocity can easily be determined and can be expected to remain constant along the span. For a centrifugal impeller, similar conditions apply even though robust three-dimensional flow effects due to the deceleration of fluid along the impeller blades, deflection effects and boundary layer effects need to be considered. Applying least-mean-square fitting to the extracted limiting frequencies allows the identification of a first representative velocity and scaling with the circumferential velocity of the impeller. The summary in Table 4 shows a meaningful fit and gives the first hint that destructive interference is a determining effect for maximum noise reduction. On the other hand, destructive interference usually accompanies constructive interference at frequencies approaching $\Delta\varphi = 2\pi$; the same is observed for frequencies exceeding the design frequency $f > f_{D,max}$, leading to a significant noise increase ($\Delta SPL < 0$; Fig. 9). The challenge is to design a porous setup, where the designed destructive interference effects are located in the relevant and reinforced spectral A-weighting region, resulting in maximum overall (A-weighted) noise reduction as shown in Fig. 8 (b and d).

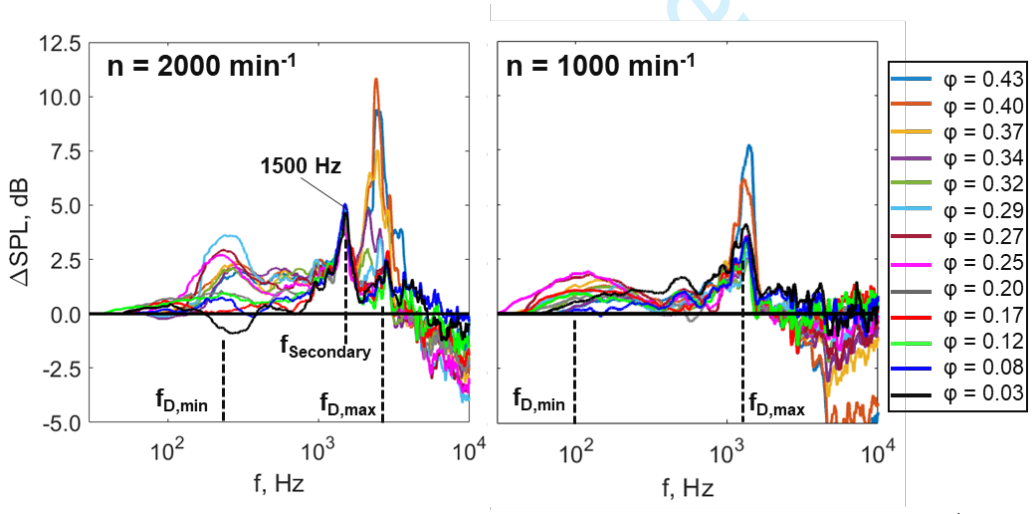

Figure 9: Spectral noise reduction at variable fan speed along the full characteristic fan curve at n = 1000 min^{-1} (left) and n = 2000 min^{-1} (right). C_P/C_0 = 40 % porous coverage. Positive quantities indicate a noise reduction relative to the reference impeller (Eq. 7).

$$f_{design} = U^{\cdot} / (2 \cdot \Delta C \cdot N)$$
$$U^{\cdot} = 0.63 \cdot U, \Delta C = 5.6 \cdot 10^{-3}, N \in [1..8] \quad (9)$$

Table 4 Spectral range of noise reduction assigned as a function of the covered surface area.

	Experimental		Analytical (Eq. 9)		Deviation
n [min^{-1}]	f_{min} [Hz]	f_{max} [Hz]	f_{min} [Hz	f_{max} [Hz]	Dev_{mean} [%]
2000	250	2418	261	2351	4
1500	192	1530	196	1763	9
1000	115	1390	131	1175	15

5. Porous Impeller: Surface Variation

This section addresses the continuous variation of the covered porous surface. Initially, the porous region of the impeller blades was fully covered using highly adhesive tape. Starting with the row closest to the impeller blade trailing edge (ΔC = 5.6 mm), an increasing number of porous rows was uncovered and exposed to the acting flow, hence continuously increasing the porous surface. This variation served the purpose of determining the optimum area of porous coverage to maintain maximum acoustic abatement while providing high aerodynamic efficiency. Moreover, the direct comparison of a fully covered porous region with the reference baseline impeller provided information regarding the effect of aeroacoustic invisibility of the tape used while providing aerodynamically beneficial conditions.

5.1 Porous Surface Variation: Global Performance

Figures 10 and 11 show overall performance in terms of aerodynamics and acoustics. Generally, Figure 10 indicates highly similar aerodynamic performance for all tested cases. However, a careful analysis of the total pressure rise shows the reference impeller and the impeller with a fully covered (taped) porous surface to be slightly superior to those with maximum porosity (8 rows) along the entire characteristic curve. This trend is quantifiable using maximum differences of $\Delta\Psi = 1.4\%$ and $\Delta\eta = 0.3\%$, where especially the latter falls within the range of uncertainty of the conducted experiments (Table 2). Local separation at the perforated holes is expected to slightly alter the boundary layer structure on the rear part of the impeller blades, causing an effect on the angle of incidence at the blade trailing edges. On exposing an increased area of porosity to flow (increasing the number of rows), the disruptive separation effect extended and migrated upstream from the trailing edge in the direction of the leading edge. The associated increase in drag shows the potential to increase shaft power and hence aerodynamic efficiency even though the latter remains almost undetectable in the investigated cases. Note that a slight difference is observed in the fan efficiency of the maximum porous configuration when comparing Fig. 10 with Fig. 7 under identical conditions. This reduction in efficiency can be ascribed to the preliminary nature of the measurements presented in Fig. 7. After mounting the new fan setup, a grinding seal temporarily caused increased torque values at the driving shaft for the first experimental run, hence affecting the accuracy of this measurement. Since this artefact was first observed during the signal analysis post running the experimental campaign, a repeated testing of the same configuration was not manageable.

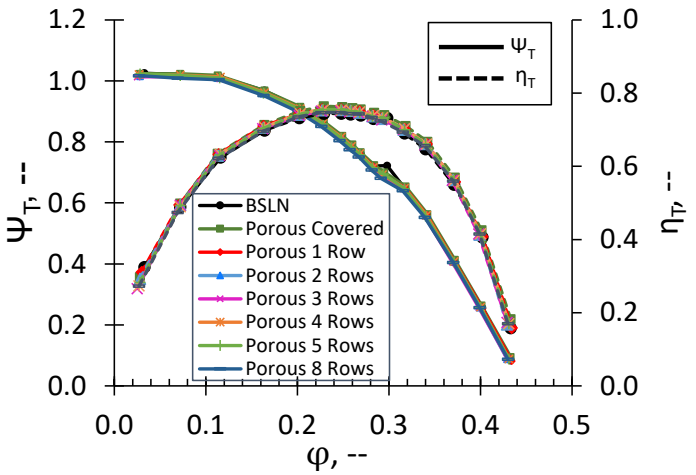

Figure 10: Aerodynamic performance for variable porous surfaces (row numbers) with n = 2000 min^{-1}.

An increased effect of the porous surface area, however, can be obtained from the overall acoustic level distribution as shown in Figure 11. The baseline reference case generally defines the upper limit for all evaluations along the entire characteristic curve. However, analysing non-weighted overall level (Fig. 11 a) or OSAPL according to the method described by Madison et al. [16] and incorporating aerodynamic performance (Fig. 11 c) provided some general benefits that were especially close to design conditions but no clear ranking of the investigated porous surface could be seen. This pattern changed dramatically when applying A-weighting, hence the focus on the mid-frequency range of 1 kHz ≤ f ≤ 6 kHz (Fig. 11 b). Along the entire working range of the centrifugal fan, a series of curves that scaled with the number of (un)covered porous rows from the baseline (max levels) towards fully uncovered (min levels) emerged. Maximum differences were obtained at overload (ΔOASPL = 2.9 dB(A)) and design conditions (ΔOASPL = 2.5 dB(A)). The higher the surface exposed to the flow regime, the higher the associated noise reduction in the A-relevant frequency range. Surprisingly, when compared to the baseline case without any porous treatment, the porous impeller with all porous rows covered with adhesive tape still yielded a significant noise reduction of ΔOASPL = 1.9 dB(A) at design and ΔOASPL = 1.0 dB(A). Even though significantly lower than the attainable maximum, this observation reveals that when the applied tape covers the porous holes, it causes a certain degree of aeroacoustic invisibility. With no local separation possible due to the discrete holes, a purely aeroacoustic interference effect is expected to contribute to the observed noise reduction. This might offer new perspectives of practical application, where covering the holes can offer protection against the risk of clogging and hence practically ineffective applications. Since the observed trends are most distinct when analysing A-weighted levels, high practical relevance is expected, thus providing a motive for further spectral analysis of the obtained signals to identify underlying mechanisms.

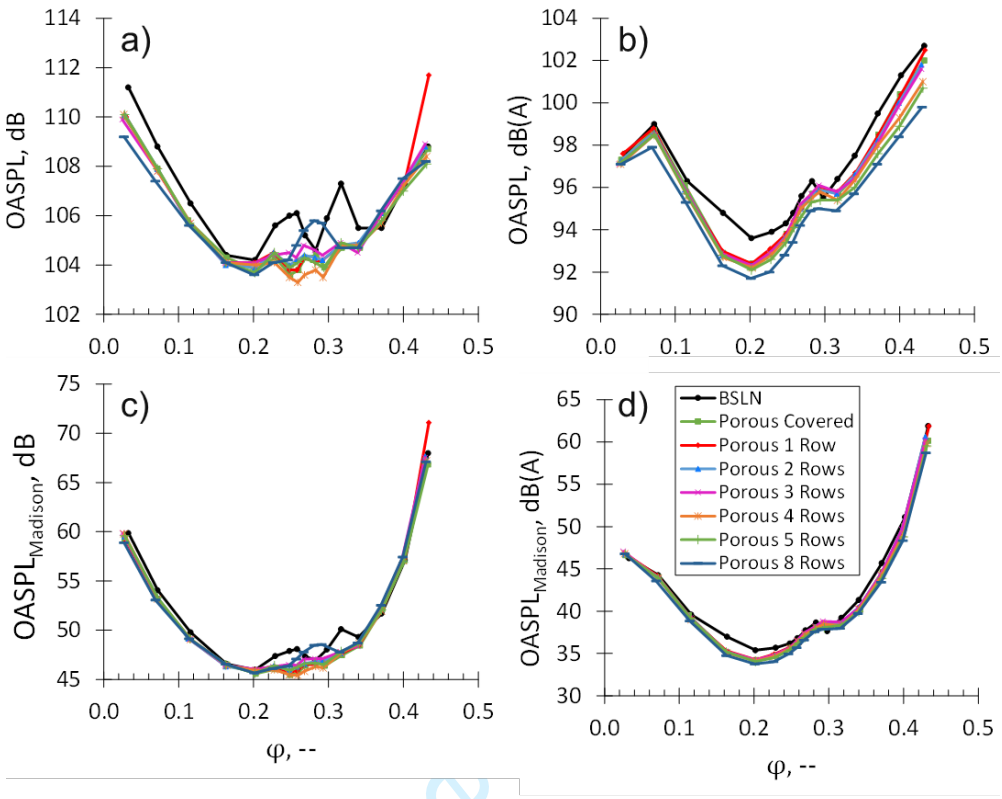

Figure 11: Aeroacoustic response at variable coverage of porous surface at n = 2000 min^{-1}. Non-weighted (a,c) and A-weighted (b,d) sound pressure level.

5.2 Porous Surface Variation: Spectral Composition

Figure 12 shows the effect of porous blade treatment at fan design conditions while varying the fan speed. Here, a clear scaling of the noise reduction pattern with the number of porous rows is observed; and this scaling primarily affects maximum noise reduction amplitudes, while the addressed frequency band remains rather unaffected by the number of rows covered. These specific observations at design conditions indicate that the upper spectral limit of noise reduction is mainly a function of the chordwise distance between the blade trailing edge and the first porous row that is closest to the trailing edge according to Eq. 9. In reverse conclusion, the upstream rows rather interact with their neighbouring upstream or downstream rows than with the trailing edge far downstream, which would alter the effective spectral range. This meets the results of the single aerofoil (Section 3, Fig. 6), where the chordwise spacing shows little interaction effects but solely an additional contribution to the total noise reduction. The low frequency shows indistinct dependencies but the noise-reduction effectiveness at low frequencies increases as the porous surface is extended. It is also clear from Eq. 9 that varying the fan speed results in a shift of frequency where the peak noise reduction takes place. However, at design conditions, $\varphi = 0.25$; the representative velocity differs from $U^* = 0.63 \cdot U$ as stated in Eq. 9 but varies from $U^* = 0.40 \cdot U$ for n = 2000 min^{-1} to $U^* = 0.71 \cdot U$ for n = 1000 min^{-1}, which is mainly due to the absence of the reduction-dominating secondary peak in Fig. 9 that is only present at overload conditions or low blade inflow angles, respectively (also discussed in Fig. 14).

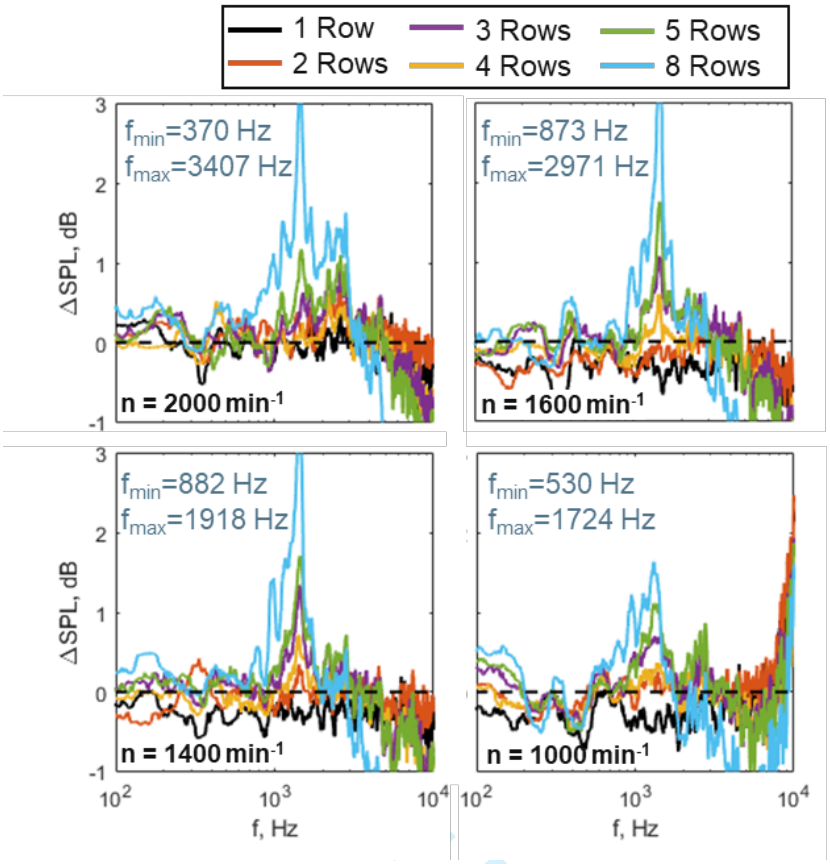

Figure 12: Trend of noise reduction at design conditions $\varphi = 0.25$ and varying covered porous surfaces (number of rows). Positive quantities indicate a noise reduction relative to the reference impeller (Eq. 7).

In assessing the relevance of the applied porous surface, Figure 13 exemplarily shows a surface-specific effect on the noise reduction capacity at variable fan speed. The results indicate that at least three porous rows need to be exposed to the flow to obtain significant spectral noise reduction. Even though the first row seems to determine the covered spectral range, an effect on the total noise reduction is not detectable. This changes when the covered surface area increases, suggesting a combined effect of destructive interference and noise attenuation due to porosity. Maximum noise reduction is achieved by exposing the maximum surface (all rows) to flow, and no saturation effect is observed (Fig. 13), motivating future tests with a porous coverage extending towards the impeller blade leading edges.

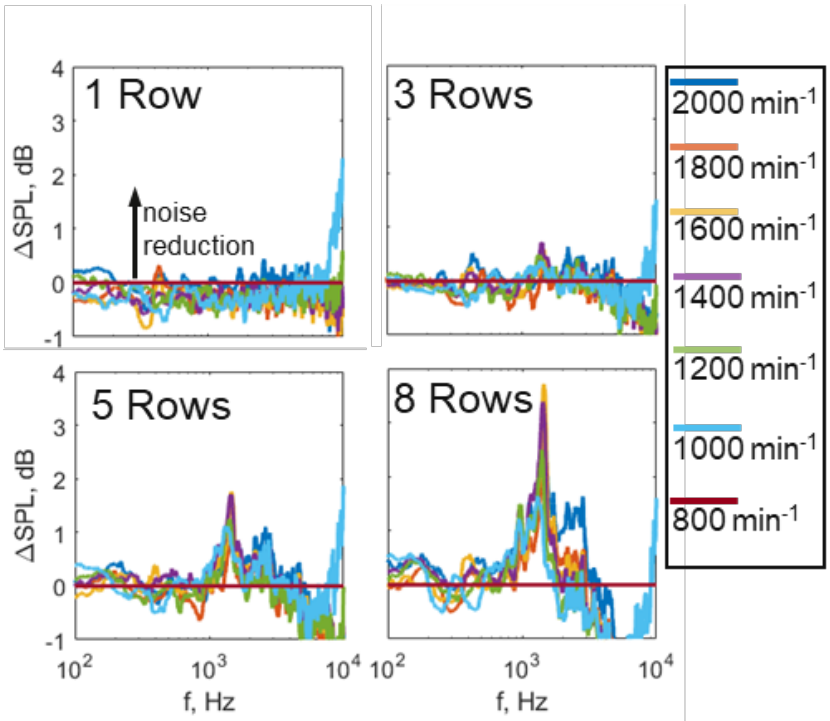

Figure 13: Spectral noise reduction at design conditions φ = 0.25 for varying porous surfaces and rotational speeds. Positive quantities indicate a noise reduction relative to the reference impeller (Eq. 7).

The trends observed in Figure 13 were reconfirmed when the operating range was extended towards overload and part-load conditions as seen in Fig. 14. Analysing the effect of different operation points on the noise reduction potential of perforated blades showed two primary effects. First, the aeroacoustic performance tended to scale with the number of porous rows in general, whereas secondary and primary reduction took place under overload and part-load conditions, respectively. Even though still significant, the effect of the porous surface treatment decreased at design conditions (φ = 0.25). The upper limit of the spectral noise reduction scaled with the aerodynamic state of the impeller blades as well. At overload, minimum angles of incidence were obtained at the leading edge, primarily causing separation effects on the suction side of the blades, while the pressure side was fully attached. As a consequence, the effective spectral range shifted towards low frequencies, allowing a reduction of the interaction of large-scale separated structures with the impeller surface. This also led to a significant noise reduction of up to 10 dB at the design frequency. This is consistent with the mean effects shown for the single aerofoil in Fig. 6a, where minimum angles of attack predicted the maximum noise reduction capacity. At part-load, the angles of incidence increased, with a separation of the impeller pressure side as a consequence. This shifted the entire spectral range towards high frequencies, which can be ascribed to a reduction in the level of high-frequency noise of the reference impeller. In terms of magnitudes, however, the noise reduction capacity at part-load, compared to the capacity at overload conditions (Fig. 14 c), decreased – once again in agreement with Fig. 6. Design frequency, as indicated by peak-noise reduction, shifted from 2409 Hz for overload conditions to 1482 Hz at design and part-load (1502 Hz) conditions. This served as an indicator of early separation on the pressure side of the blade, making the last porous rows superfluous regarding their noise reduction capacity. Since no attached flow regime existed towards the trailing edge of the impeller blade, an upstream row served as a determining artefact that specified the design frequency as stated in Eq. 9.

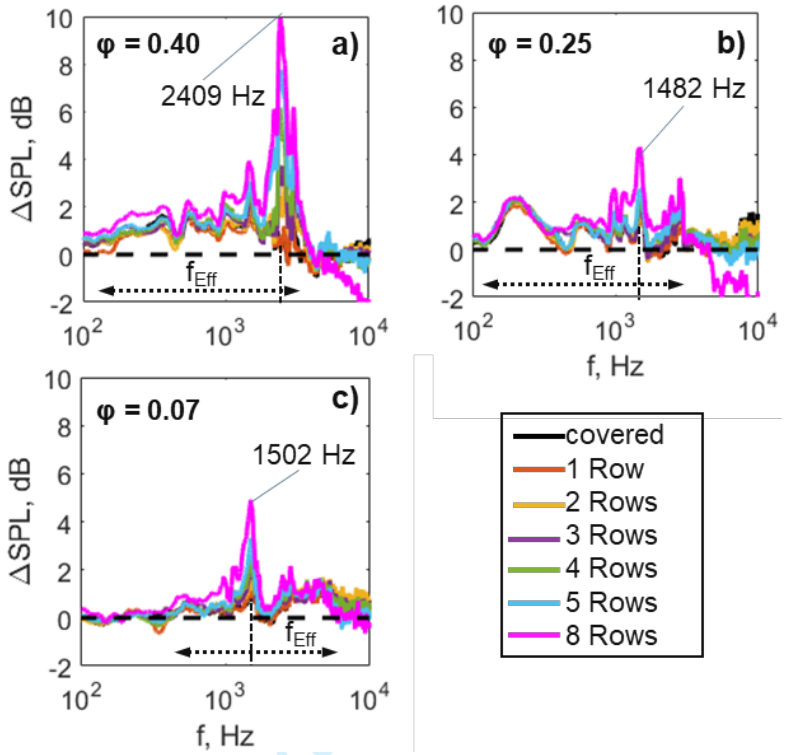

Figure 14: Spectral noise reduction as a function of the operating point at a) overload, b) design and c) part-load conditions. Positive quantities indicate a noise reduction relative to the reference impeller (Eq. 7).

6. Conclusion

Porous treatment was applied to a single stationary aerofoil and a centrifugal fan impeller. Then a comparative study of these cognitional devices was performed, allowing the detection of common characteristics in terms of noise reduction. With regard to analysis, both time and spectral domain were assessed to identify global effects as well as to uncover underlying noise reduction mechanisms. For the centrifugal impeller, the effects of various operation conditions, variable speeds and the covered porous surface were examined and led the current research to obtain the following conclusions:

- Lower and upper frequency bands of noise reduction scale with the distance between the blade trailing edges and the first porous rows relative to a characteristic relative velocity. This serves as an indicator of the existence of destructive interference effects of either aerodynamic and/or aeroacoustic nature. For the rotating application, a scaling law can be proposed, considering the streamwise spacing of the pores as well as the number of porous rows applied.

$$f_{design} = \frac{U^*}{2 \cdot \Delta C \cdot N}$$

- Compared to the reference impeller, fully covered porous surfaces also show a noise reduction ability, which is ascribed to the aeroacoustic invisibility of the applied coverage, hence allowing aeroacoustic interference effects between porous treatment and a trailing edge.

- A-weighted levels especially showed a clear scaling of the noise reduction pattern with the surface of porosity. Significant benefits were obtained with at least 3 porous rows exposed to the flow field even though no saturation effects appeared to be present at the tested maximum of 8 rows or 40% coverage.

- The most effective noise reduction occurred during overload conditions $\Delta OASPL_{Overload}$ = 2.9 dB(A) and at design conditions ($\Delta OASPL_{Design}$ = 2.5 dB(A)) of the fan. The trends remain qualitatively unchanged even when aerodynamically deviant operating conditions are compensated.

- Aerodynamic fan performance was slightly affected by the existence of porosity in general although the performance remained almost unaffected by varying the area of porosity. Especially in contrast to previously tested single aerofoils, this performance tended to increase the positive potential of the application of porosity in rotating machinery.

- Aerodynamic penalties in terms of the static pressure rise amount to $\Delta(\Delta pT) = -1.01$ % on average. However, in terms of efficiency, the porous impellers on trend show a constant performance, speaking for a reduced associated shaft power. In the current study, the latter differences are thought to be of too little significance to conclude on the associated effects and need to be further investigated.

- Even though the total noise reduction proves to be existent along the entire characteristic curve, aeroacoustic penalties can be seen in the spectral composition, where the speed-dependent self-noise of the pores lead adds to potential constructive interference effects, leading to a local increase of the acoustic levels, starting from $f \geq 3600$ Hz at $n = 2000$ min^{-1} and $f \geq 2100$ Hz at $n = 1000$ min^{-1}. This pattern highlights the need to choose the porous parameters carefully to maintain a maximum total noise reduction, especially when considering weighting functions.

- The existence of comparable trends between a single aerofoil and a centrifugal fan concerning jet velocity (circumferential speed), AoA (operation point), and a covered porous surface can be qualitatively confirmed.

Acknowledgments

The authors would like to express their gratitude to Pollrich Fan Factories, Mönchengladbach/ Siegen for providing the test facility and the opportunity to conduct the experiments. The authors would also like to thank the Engineering and Physical Sciences Research Council in the United Kingdom through research grant No. EP/V006886/1, and the PhD studentship sponsored by the Doctoral Training Partnership.

References

1. Eck B. *Ventilatoren, Entwurf und Betrieb der Radial-, Axial- und Querstromventilatoren*, 6th ed., Berlin, Germany: *Springer Verlag*, 2003, ISBN 978-3-642-55650-0.
2. Neise W. Noise reduction in centrifugal fans: A literature survey. *Journal of Sound and Vibration* 1976; 45(3): 375-403
3. Graham R R. The silent flight of owls. *Journal of the Royal Aeronautical Society* 1934; 38(286): 837–843. DOI: 10.1017/s0368393100109915.
4. Sarradj E, Fritzsche C, Geyer T. Silent owl flight: Bird flyover noise measurements. *AIAA Journal* 2011; 49(4): 769–779. DOI: 10.2514/1.J050703.
5. Geyer T, Sarradj E, Fritzsche C. Measurement of the noise generation at the trailing edge of porous airfoils. *Experiments in Fluids* 2009; 48(2): 291–308. DOI: 10.1007/s00348-009-0739-x.
6. Geyer T, Sarradj E, Fritzsche C. Porous Airfoils: Noise Reduction and Boundary Layer Effects. *International Journal of Aeroacoustics* 2010; 9(6):787-820. DOI: 10.1260/1475-472X.9.6.78
7. Geyer T, Sarradj E. Trailing edge noise of partially porous airfoils. In: *20th AIAA/CEAS Aeroacoustics Conference*, Atlanta, USA, 16-20 June 2014, paper no. AIAA 2014-3039. Reston: AIAA. DOI: 10.2514/6.2014-3039.
8. Zhang M, Chong T P. Experimental investigation of the impact of porous parameters on trailing-edge noise. *Journal of Sound and Vibration* 2020; 489: 115694. DOI: 10.1016/j.jsv.2020.115694.
9. Carpio A R, Martínez R M, Avallone F, Ragni D, Snellen M, van der Zwaag S. Experimental characterization of the turbulent boundary layer over a porous trailing edge for noise abatement. *Journal of Sound and Vibration* 2019; 443: 537–558. DOI: 10.1016/j.jsv.2018.12.010.
10. Scholz M, Biedermann T M, Chong T P, Smith E. Statistical modelling of aerofoil self-noise subjected to structured porous trailing edges. In: *Proceedings of 28th AIAA/CEAS Aeroacoustics 2022 Conference*, Southampton, UK, 14-17 June 2022, paper no. AIAA 2022-3092. Reston: AIAA. DOI: 10.2514/6.2022-3092
11. Biedermann T M, Chong T P, Kameier F, Paschereit C O. Statistical-empirical modelling of airfoil noise subjected to leading edge serrations. *AIAA Journal* 2017; 55(9): 3128–3142. DOI: 10.2514/1.J055633

12. ISO 5136:2003. Acoustics – Determination of sound power radiated into a duct by fans and other air-moving devices – In-duct method.
13. ISO 5801:2007. Industrial fans – Performance testing using standardized airways.
14. Biedermann T M, Moutamassik Y, Kameier F. Assessment of the impeller/volute relationship of centrifugal fans from an aerodynamic and aeroacoustic perspective, In: *ASME Turbo Expo Turbomachinery Technical Conference and Exposition*, Rotterdam, NL, 13-17 June 2022, paper no. GT2022-79389, New York: ASME. DOI: 10.1115/GT2022-79389
15. The Federal Government. Sechste Allgemeine Verwaltungsvorschrift zum Bundes-Immissionsschutzgesetz, (Technische Anleitung zum Schutz gegen Laerm – TA Laerm). Germany, 2017; § 48 BImSchG, IG I 7 – 501-1/2.
16. Madison, R D. *Fan Engineering (Handbook)*, 5th ed., Buffalo, New York: Buffalo Forge Company, 1949
17. Bommes L, Fricke J, Grundmann, R. *Ventilatoren*, 2nd ed. Essen, Germany: Vulkan Verlag, 2002, ISBN 3-8027-3200-6.
18. Bohl W, Elmendorf, W. *Stroemungsmaschinen I*, 11th ed. Wuerzburg, Germany: Vogel Buchverlag, 2013, ISBN 978-3-8343-3288-2.
19. Schade H, Kunz E, Kameier F, Paschereit C O. *Strömungslehre*, 4th ed., Berlin, Germany: DeGruyter, 2013, DOI: 10.1515/9783110292237